Int. J. Pres. Ves. & Piping **19** (1985) 83–99

A Strain Hardening Failure Assessment Diagram Derived from Carbon–Manganese Steel Compact Tension Specimens

R. Bradford, R. S. Gates, G. Green & D. C. Williams

Central Electricity Generating Board, South Western Region,
Bedminster Down, Bridgwater Road, Bristol BS13 8AN, Great Britain

(Received: 13 February, 1984)

ABSTRACT

A failure assessment diagram is derived from carbon–manganese steel compact tension specimens. The diagram has been determined from an elastic–plastic finite element analysis of a compact tension specimen geometry. The diagram has been validated by using experimental fracture toughness data obtained on the same steel and specimen geometry modelled in the finite element analysis. The plastic collapse load has been determined empirically for this geometry.

It is shown that a non-work-hardening failure assessment diagram is not a good representation of the experimental data and that the computed failure assessment diagram is more appropriate for describing the behaviour of the carbon–manganese steel specimens.

NOMENCLATURE

a	Crack length.
Δa	Crack growth.
A	Crack area $= Ba$.
B	Specimen thickness.
E	Young's modulus.
J	J contour integral.
J_e	Elastic part of J.
J_m	Value of J at maximum load.

Int. J. Pres. Ves. & Piping 0308-0161/85/$03·30

K_i Stress intensity factor for crack initiation.
K_m Stress intensity factor at maximum load.
K_r Ratio of applied stress intensity factor to fracture toughness.
n Work hardening exponent.
P Applied load.
$P_{collapse}$ Plastic collapse load.
P_f A reference load.
P_i Crack initiation load.
P_m Maximum load.
P_N Normalised applied load.
S_r Ratio of applied load to reference collapse load.
U Area under load–displacement curve.
W Specimen width.

ν Poisson's ratio.
σ_f Flow stress $= (\sigma_y + \sigma_u)/2$.
σ_o Limit of proportionality.
σ_u Ultimate strength.
σ_y Yield stress.

FAD Failure Assessment Diagram.
FE Finite Element.

1. INTRODUCTION

During periodic inspections of structures, defects may be frequently detected and an assessment of the integrity of the structure may be required. Knowledge of the load, crack length and material properties such as fracture toughness and tensile strength when combined with a failure assessment diagram (FAD) will allow the assessor to estimate the proximity of the structure to failure.

Previously, an FAD was proposed which was geometry and material independent.[1] Whilst the full R6 procedure involves the use of lower bound data and collapse solutions for conservatism, and hence is a failure avoidance procedure, the R6 assessment diagram itself may also be interpreted as a predictive tool for materials with an elastic–perfectly plastic behaviour when used in conjunction with realistic data. However, subsequent investigations[2–4] have examined the influence of material strain hardening on the shape of the FAD and have demonstrated a

strong effect of this parameter. Studies comparing experimental results and FADs have been restricted to alloy steels and austenitic steels. Since carbon–manganese steel is perhaps the most common structural material and is strongly strain hardening, it is pertinent to determine an FAD for such materials. This paper describes the derivation and validation of an FAD derived from laboratory compact tension specimens, as a first stage in developing an FAD applicable to general structures.

2. FAILURE ASSESSMENT DIAGRAMS/METHODS

The FAD technique involves calculating the parameters K_r and S_r for a structure. K_r is defined as $\sqrt{J_e/J}$ where J_e is given by $(1-\nu^2)K^2/E$ in plane strain and J is a critical value of the J-integral.[5,6] K is the elastic stress intensity factor, E is Young's modulus and ν Poisson's ratio. J has been shown to characterise the crack tip stress/strain field even beyond general yielding in bend geometries.[7–9] The critical J value can be chosen to represent the onset of crack growth or a J value corresponding to some amount of stable ductile tearing if the material is ductile.

S_r is defined as some reference stress related to a critical event such as yield or collapse and is defined as P/P_f, where P_f is some reference load to be discussed later.

The locus of K_r/S_r values calculated in assessments using appropriate critical J and P_f values is then compared with an assessment line. Those values which lie outside the line imply crack extension, and therefore reaching the line implies the initiation of crack growth. This proceeds until the locus of K_r/S_r values calculated for increasing crack length and allowing for the tearing resistance becomes tangential to the FAD.[10] Instability occurs at this point.

The FAD technique is essentially a J-estimation technique which avoids having to perform a full elastic–plastic analysis of the structure. The technique relies upon the ratio of J_e/J (which defines the assessment line) being unique at the same P/P_f ratio in different structures of the same material. The choice of P_f is therefore critical in determining structural stability.

There is some confusion concerning the choice of an appropriate S_r value and hence P_f. Often the collapse solution and collapse stress are determined empirically and it is not possible to decouple the collapse

solution from the collapse stress. In some cases the global collapse load may not be the appropriate choice and a local collapse stress or collapse solution may be required.

It is convenient to define S_r as

$$S_r = \frac{P}{P_{\text{collapse}}} \times \frac{\sigma_u}{\sigma_f}$$

where the 'flow stress' σ_f is defined as $(\sigma_y + \sigma_u)/2$. This definition minimises the effect of strain hardening on the FAD since the maximum distance apart of the line for a given σ_u/σ_y ratio and the line for $\sigma_u/\sigma_y = 1$ is made as small as possible. This point will be discussed at length later.

3. DERIVATION OF THE FAILURE ASSESSMENT DIAGRAM

Since a considerable body of data was available from laboratory tests on compact tension specimens of structural carbon–manganese steels, it was decided to derive an FAD for this geometry and a specific steel typical of those examined. The mechanical properties and chemical composition of the steel are given in Table 1.

3.1. Finite element analysis

The mesh employed is shown in Fig. 1, only half the specimen being modelled by virtue of symmetry. The dimensions are W (width) 50 mm, B (thickness) 25 mm. The program used, BERSAFE PHASE III, is described in Ref. 11. Briefly, it is based on incremental plasticity with isotropic hardening, and uses infinitesimal strain theory. Quadratic, isoparametric elements were used in the mesh. This was loaded by applying a displacement in the y direction to the node C on the

TABLE 1
Composition and Mechanical Properties of Carbon–Manganese Steel Used in Finite Element Calculations

Chemical composition (wt %)								σ_y	σ_u
C	*Cr*	*Cu*	*Mn*	*Ni*	*P*	*Si*	*S*	$(MN m^{-2})$	$(MN m^{-2})$
16	0·07	0·14	1·13	0·07	0·015	0·27	0·04	225	429

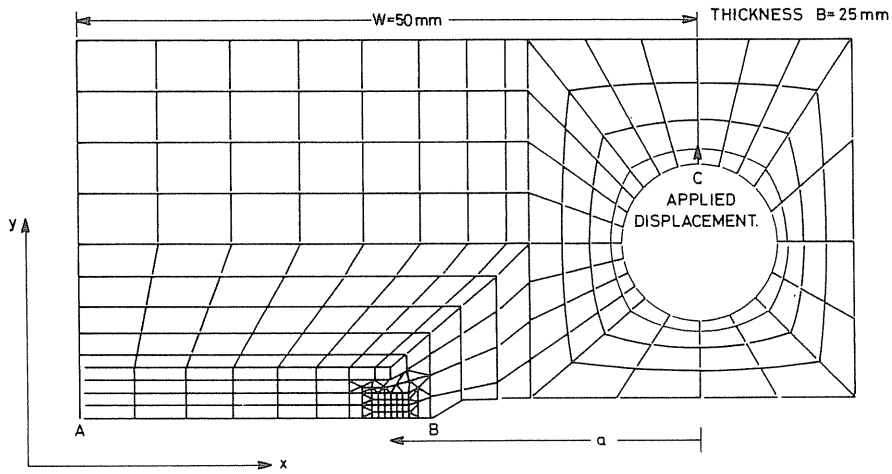

Fig. 1. Mesh of compact tension specimen.

circumference of the loading hole shown in Fig. 1. Because of symmetry, the nodes along the ligament AB (Fig. 1) were fixed in the y direction. The node A was fixed in the x direction to remove the rigid body degree of freedom.

The elements adjacent to the loaded node C were given an artificially high yield stress to suppress yielding local to the loading hole. The remaining elements were given the stress–strain behaviour shown in Fig. 2. These data were obtained from tensile tests on the C–Mn steel, and the characteristic stresses are:

ultimate	$\sigma_u = 429$ MPa
0·2% proof	$\sigma_y = 255$ MPa
limit of proportionality	$\sigma_o = 210$ MPa

The stress–strain curve is not of power law form, and attempts to fit to this form gave a hardening index n anywhere between 3·5 and 6·5.

Calculations were performed for three crack length/width (a/W) ratios of 0·50, 0·51 and 0·524. Plane stress out-of-plane constraint was assumed. The resulting load–displacement curves are shown in Fig. 3. The displacement is that of one loading hole relative to the other. An experimental load–displacement curve is shown in Fig. 4, corrected for extraneous deflections, for which a/W varied due to stable tearing from 0·502 to 0·517. The appropriate interpolation of the FE results is also shown in Fig. 4, and agrees quite well with experiment.

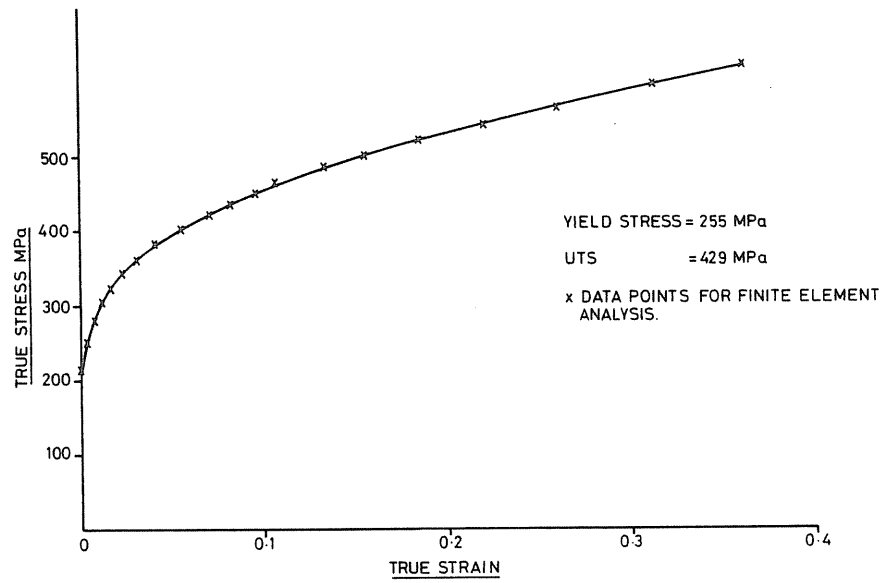

Fig. 2. True stress–true strain curve used in the analysis.

J has been calculated using its interpretation as an energy release rate:

$$J = \frac{1}{B}\frac{\partial U}{\partial a}$$

where U is the area under the load–displacement curves shown in Fig. 3, the derivative being carried out at constant displacement. In principle, this definition of J, and the definition as a path integral, may differ slightly for incremental plasticity. However, for monotonic loading this difference is probably slight and has been ignored. In the elastic regime a normalised stress intensity factor $F(a/W)$ may be defined by

$$F(a/W) = \frac{KB\sqrt{W}}{P}$$

where P is the applied load. For $a/W = 0{\cdot}505$ the FE analysis gives $F = 9{\cdot}77$ which is within $0{\cdot}6\,\%$ of the result given by Neumann.[12] In the fully plastic regime we find that J is given by

$$J = \frac{2{\cdot}09\,U}{B(W-a)} \qquad \text{for } a/W = 0{\cdot}505$$

The numerical coefficient in the above expression is smaller than that

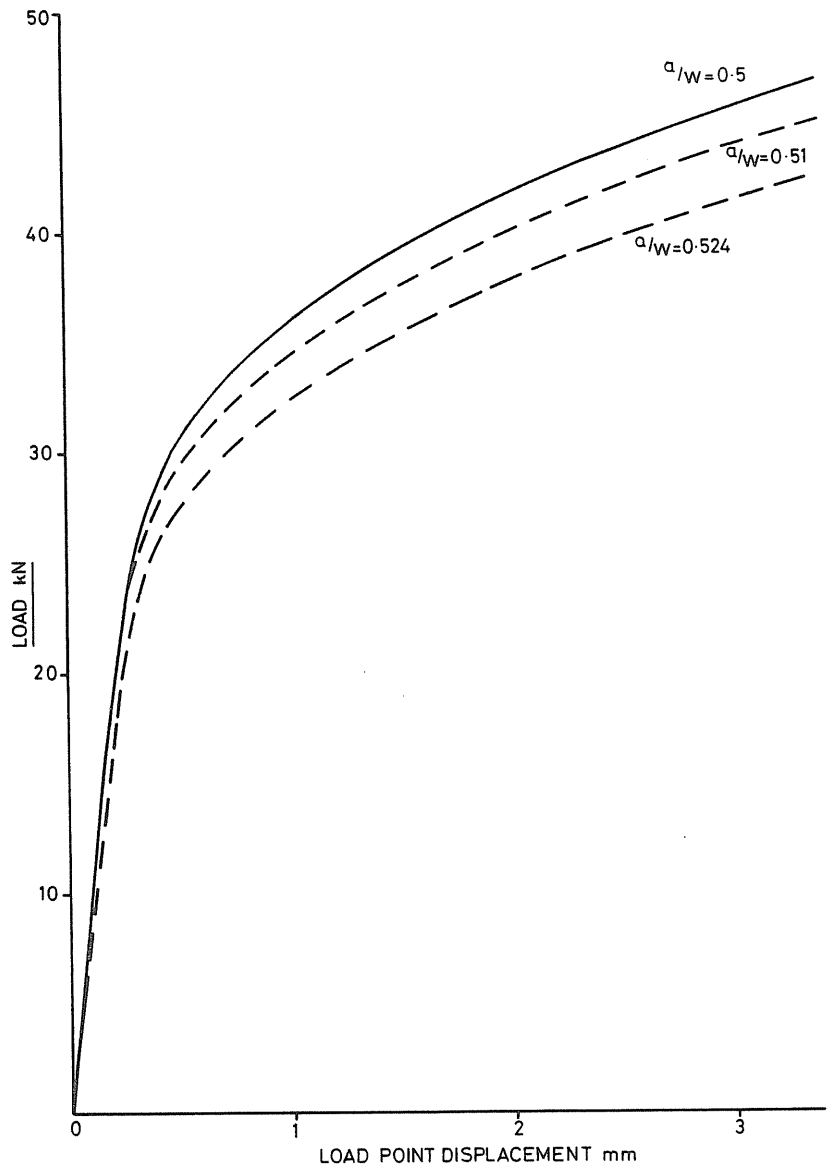

Fig. 3. Calculated load–displacement curve for plane stress and various a/W.

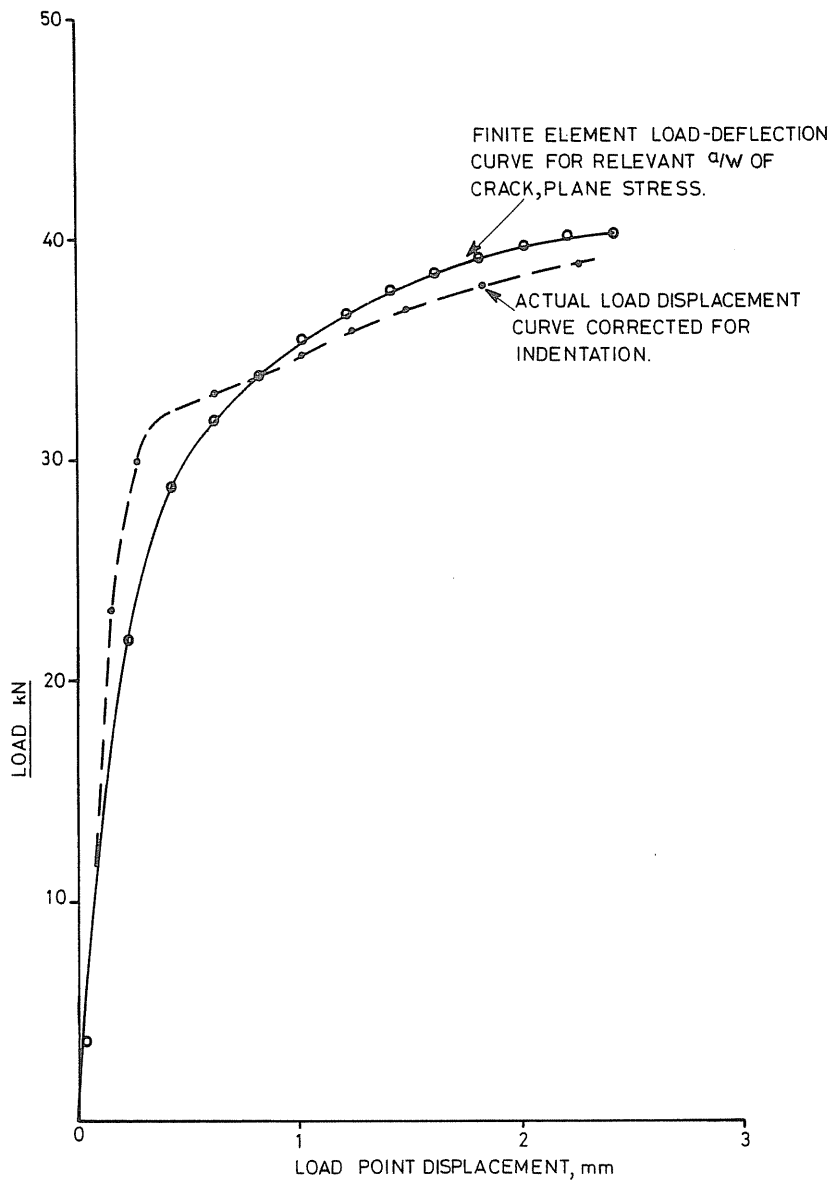

Fig. 4. Comparison of actual and calculated load–displacement curves.

given by Merkle and Corten[13] by 8%. However, our term U is probably larger than that of Merkle and Corten, because no subtraction has been made of the elastic energy of the uncracked body. In addition, the point loading used leads to larger displacements, and hence larger energies. The agreement of the J values is probably, therefore, quite reasonable.

3.2. Empirical collapse solution

To convert the above J calculations to an assessment diagram, a collapse solution is required. This was determined experimentally from a series of tests on compact tension specimens containing blunt notches (radii 1·5 mm). Data were obtained from specimens which did not exhibit crack growth prior to collapse. A normalised collapse load is defined by

$$P_N = \frac{P_{collapse}}{BW\sigma_u}$$

and the values of P_N for $a/W = 0{\cdot}40$, $0{\cdot}50$ and $0{\cdot}60$ are given in Table 2. P_N was found to be the same for both 5 mm and 25 mm thick specimens of constant 50 mm width, which implies collapse under plane stress conditions. For comparison, Table 2 also shows the values of P_N from

TABLE 2
Comparison of Candidate Limit Load Solutions with Experiment

(*a*) *Plane strain limit load solutions*

a/W	$P/BW\sigma$ *Haigh and Richards*[16]	$P/BW\sigma$ *Merkle and Corten*[17]	$P/BW\sigma_u$ *experimental*
0·40	0·199	0·179	0·151
0·50	0·129	0·118	0·098
0·60	0·076	0·072	0·066

(*b*) *Plane stress limit load solutions*

a/W	$P/BW\sigma$ *Haigh and Richards*[16]	$P/BW\sigma$ *Ford and Lianis*[18a]	$P/BW\sigma_u$ *experimental*
0·40	0·123	0·142	0·151
0·50	0·081	0·092	0·098
0·60	0·046	0·055	0·066

[a] This is a solution for pure bending.

theoretical analysis in plane stress and plane strain. The plane stress results are found to be lower bounds, while the plane strain results are overestimates.

3.3. The resulting diagram

An assessment diagram can be drawn on the basis of the finite element calculation of J, the empirical collapse solution and the definition of S_r given in Section 2. This is shown in Fig. 5, and applies to the material with the stress–strain behaviour shown in Fig. 2, and in particular for $\sigma_u/\sigma_y = 1{\cdot}68$. Note, however, that the ultimate/proportionality limit ratio is larger, 2·04.

The dashed curve in Fig. 5 shows the probable position of the assessment curve for an elastic–perfectly plastic material ($\sigma_u/\sigma_y = 1$). This curve is that of Milne *et al.*[1] It can be seen that if S_r had been defined by $P/P_{collapse}$, our assessment curve would shrink to the left in Fig. 5, the dashed curve remaining unmoved, and this clearly increases the maximum discrepancy between the two. Similarly, if S_r were defined as P/P_f (general yield), our curve then moves to the right and hence increases

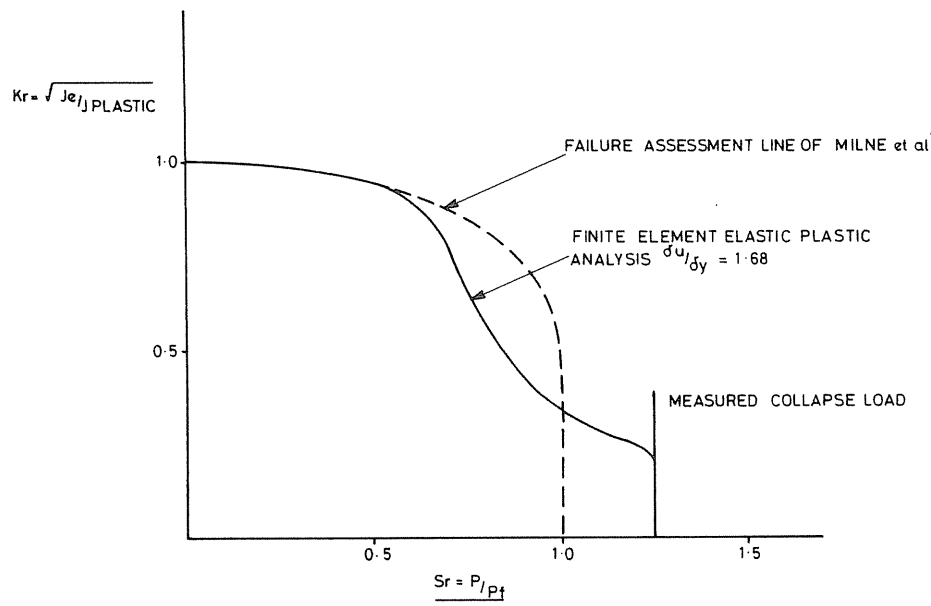

Fig. 5. Assessment curve based on measured collapse load (flow stress) and finite element dP/dA for mild steel CT specimens.

the discrepancy with the dashed curve for small K_r. Thus, as remarked in Section 2, the compromise definition of S_r, based on flow stress, minimises the strain hardening dependence of the diagram.

4. EXPERIMENTAL VALIDATION

Ductile crack growth resistance data were available for a number of carbon–manganese steels. These data were obtained in a number of specimen orientations and across a range of temperatures. Most tests were performed on 25 mm compact tension specimens. Multiple specimen tests were carried out in each case. The J value and corresponding K value, K_i, at the initiation of ductile tearing was obtained by back extrapolation of the $J/\Delta a$ crack growth resistance curve to its intersection with a blunting line. The point on any load–displacement curve corresponding to this defined initiation point could then be found through the relationship between J and the area (U) under the load–deflection curve. At this point, P_i, the LEFM stress intensity $K(P_i)$ was evaluated and hence K_r at this point on the load–deflection curve was determined from $K(P_i)/K_i$. Similarly a value of S_r has been determined, $S_r = P_i\sigma_u/P_{collapse}\sigma_f$, where the empirical collapse solution (Table 2) and the relevant material properties at the test temperature have been used. The resulting points for the C–Mn steel used in the analysis are plotted on Fig. 6 (unringed) and compared with the assessment diagram.

In addition to initiation points, maximum load points have also been plotted in Fig. 6 (ringed). These points are defined in the following way:

$$K_r = \frac{K(P_m)}{K_m}$$

$$S_r = \frac{P_m\sigma_u}{P_{collapse}\sigma_f}$$

where P_m is the load corresponding to plastic instability in tests taken to large displacements, and K_m is the tearing toughness:

$$K_m = \sqrt{EJ_m/(1-\nu^2)}$$

J_m is found from the area, U_m, under the load–displacement curve at the maximum load.

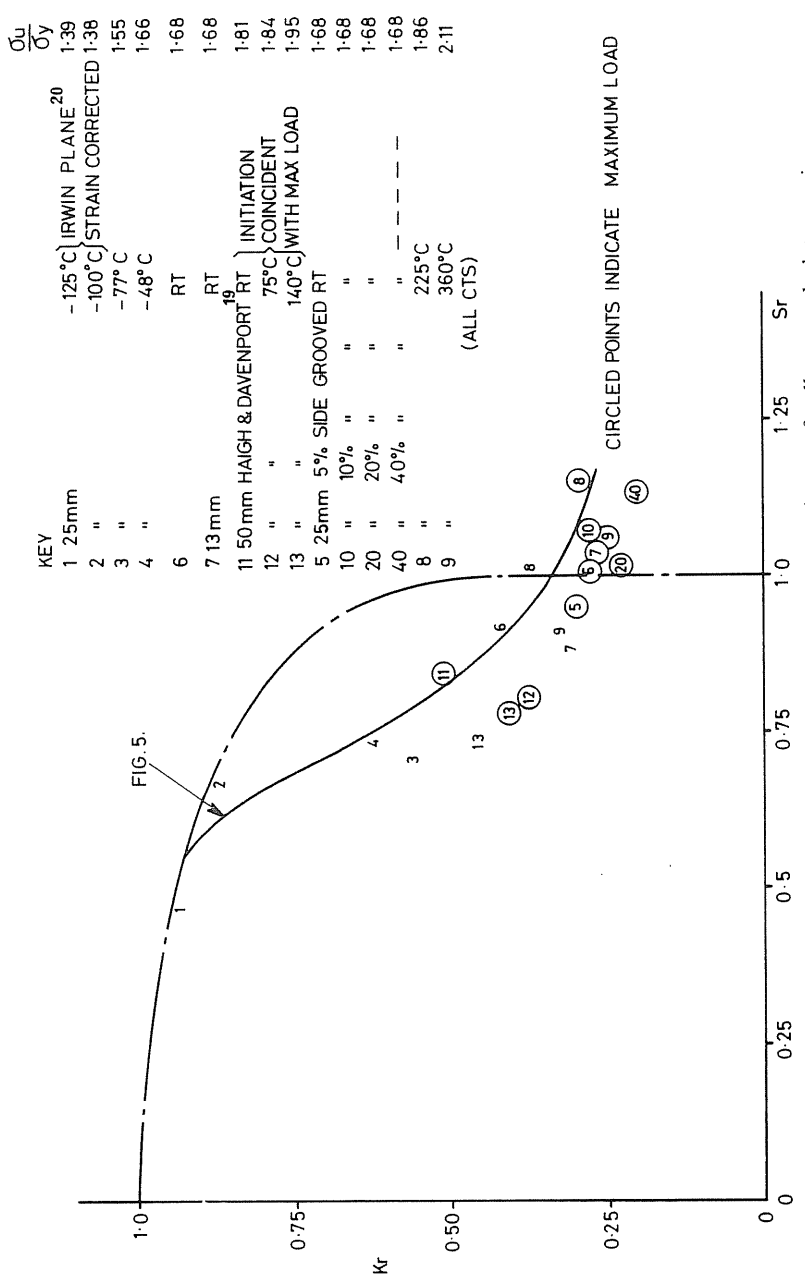

Fig. 6. Assessment line versus test data based on best estimate of collapse and plate specimens.

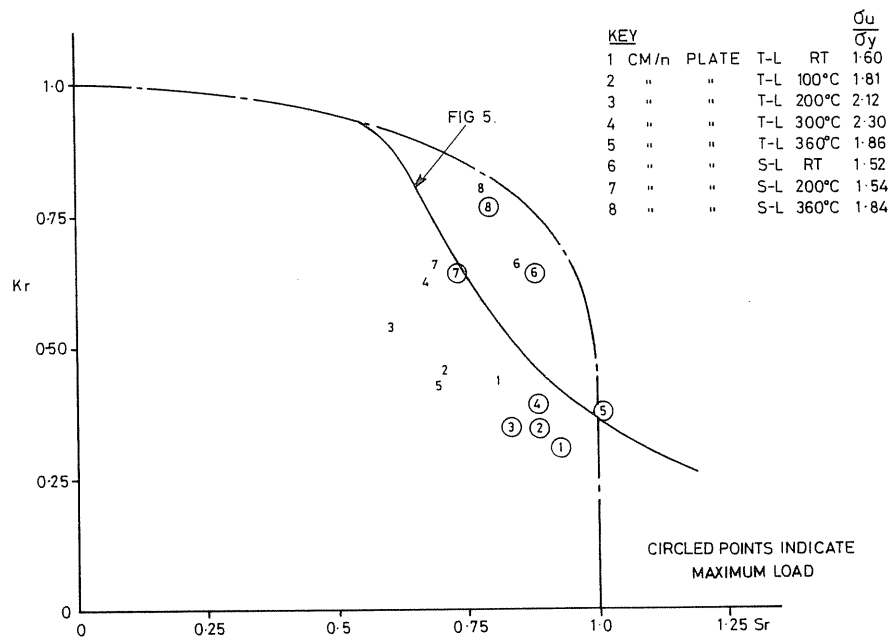

Fig. 7. Assessment line and test data based on best estimate of collapse and plate materials.

Although all the data shown are derived from compact tension specimens, several different sizes are used ($B = 13$, 25 and 50 mm) and some side grooved specimens are included. Low temperature data in which brittle fracture occurred are shown in Fig. 6 and these confirm the shape of the curve in the elastic–plastic region. There is reasonable agreement with the curve for the data relating to ductile fracture. The mean of the data lies, if anything, at a slightly lower K_r than the assessment curve. Note the agreement of the experimental data point for the conditions of the FE analysis ($B = 25$ mm, RT) with the derived FAD. Figure 6 clearly indicates that the present assessment curve is a better representation of the data than that based on a non-hardening material.

The above procedure has been repeated using data obtained on another C–Mn steel similar to that used for the FE analysis. The data are plotted in Fig. 7 for comparison with the FAD. The data scatter in a similar manner to those in Fig. 6 with a tendency to lie below the derived FAD. The scatter is greater than in Fig. 6, however, and this could be due to differences in strain hardening caused by dynamic strain ageing behaviour at the different testing temperatures. However, Figs 6 and 7

clearly demonstrate the effects of strain hardening in influencing the shape of the FAD.

5. DISCUSSION

We have shown that the assessment curve derived for the stress–strain behaviour shown in Fig. 2 differs significantly from the estimated elastic–perfectly plastic R6 curve of Milne *et al.*[1] The greater relevance of the present curve is confirmed by the experimental data.

As discussed in Section 2, the basis of the FAD technique is that a similar ratio of elastic to total J values is obtained at a similar scaled reference stress in different structures. Little information is available concerning the geometry dependence of FADs, but the concept of a J-controlled FAD implies a geometry dependence. An experimental investigation of geometry effects in FADs has been carried out for austenitic materials.[14] The results indicate a small geometry dependence with tension geometries having FADs within those of bend geometries. A similar result could be inferred using the J estimation scheme of Kumar *et*

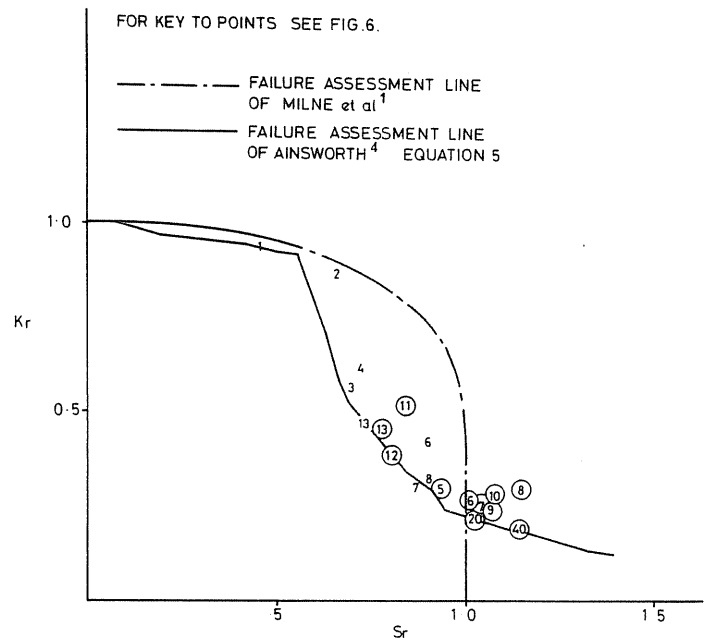

Fig. 8. Assessment line and test data based on best estimate of collapse and plate specimens.

al.[15] to derive FADs after the manner of Bloom.[2] Clearly, more work is required on the geometry dependence of FADs and the work reported here is to be extended to a tension geometry to clarify these effects. When performing assessments, the uncertainties in material properties could produce larger effects than differences in shape due to geometry. The effects of high strain hardening on the FAD appear to be much more significant than those of geometry.

In an attempt to remove the geometry dependence of FADs, Ainsworth[4] has proposed a geometry-independent diagram (eqn 5 of Ref. 4) calculated using a reference stress approach to minimise the dependence of the J estimation on the choice of strain hardening exponent when fitting a power law to stress–strain data. This curve is shown in Fig. 8 along with the data from Fig. 6. This curve is deliberately chosen to be a lower bound to the possible geometry dependence and would be expected to lie inside that for a bend geometry (compared with Fig. 6). Clearly, the data confirm that the shape of the curve is appropriate, particularly compared with the geometry-independent non-hardening curve. The combined geometry dependence and effects of strain hardening is to be examined in future work.

6. CONCLUSIONS

A failure assessment diagram has been derived using a finite element analysis of a compact tension specimen and an empirical collapse solution for this geometry.

This FAD has been validated using experimental data for the particular carbon–manganese steel used in the analysis. Fracture toughness tests on this steel and another carbon–manganese steel tested over a range of temperatures with different σ_u/σ_y ratios lie close to the derived FAD. The data are not well represented by a geometry-independent non-hardening FAD. The derived FAD, which includes the effects of strain hardening, is clearly more appropriate for describing the behaviour of compact tension specimens.

The geometry dependence of the FAD has not been explored in this paper, but the indications are that these effects are significantly less important than strain hardening on FADs. In addition to strain hardening effects, geometry dependence is to be investigated in future work.

ACKNOWLEDGEMENTS

The authors wish to acknowledge useful discussions with Dr A. T. Stewart of South West Region SSD and Dr R. A. Ainsworth of BNL. This paper is published with permission of the Director General of the CEGB (South Western Region), Bristol.

REFERENCES

1. Milne, I., Loosemore, K. and Harrison, R. P., A procedure for assessing the significance of flaws in pressurised components, *Paper C*106/78, *I.Mech.E.Conf. Publ.* (1978), 10. Mechanical Engineering Publications Ltd, London.
2. Bloom, J. M., in *Proc. EPRI Ductile Fracture Public Meeting*, Palo Alto, California, December 1980.
3. Milne, I., Fracture assessment diagrams and *J* estimates: a comparison, *Int. J. Pres. Ves. & Piping*, **13** (1983), pp. 107–25.
4. Ainsworth, R. A., The assessment of defects in structures of strain hardening material using *J* estimation procedures and failure assessment diagrams, *Berkeley Nuclear Labs Note BM/SM/EHT/20*, 1982.
5. Rice, J. R., in *Fracture*, vol. 2 (H. Liebowitz, ed.), Academic Press, New York, 1968, p. 192.
6. Eshelby, J. D., *Solid State Phys.*, **3** (1956), p. 79.
7. McMeeking, R. M. and Parks, D. M., *Elastic–Plastic Fracture*, ASTM-STP 668 (1979), pp. 175–94.
8. Shih, C. F. and German, M. D., *Int. J. Fract.*, **17** (1981), pp. 27–43.
9. Needleman, A. and Tvergaard, V., Crack tip stress and deformation fields in the solid with a vertex on its yield surface, *US Department of Energy Contract DE-AC02-80-ER10556 Tech. Rep. 87*, Brown University, 1981.
10. Milne, I., Fracture analysis in the presence of ductile crack growth, *Mat. Sci. Eng.*, **39** (1979), p. 65.
11. Hellen, T. K. and Harper, P. G., A user guide to BERSAFE Phase III Level 1 for plasticity and creep analysis, *Berkeley Nuclear Labs Report RD/B/N3597*, 1967.
12. Neumann, J. C., *Fracture Analysis*, ASTM-STP 560 (1974), pp. 105–21.
13. Merkle, J. G. and Corten, H. T., *Trans. ASME, J. Pres. Ves. Tech.*, **96**(4) (1974), pp. 286–92.
14. Akhurst, K. N. and Milne, I., Failure assessment diagrams and *J* estimates: validation for an austenitic steel, *Int. Conf. on Application of Fracture Mechanics to Materials and Structures*, Freiburg, June 1983.
15. Kumar, V., German, M. D. and Shih, C. F., An engineering approach for elastic–plastic fracture analysis, *EPRI Report NP 1931*, 1981.
16. Haigh, J. R. and Richards, C. E., *CEGB Report RD/L/M461*, 1974.

17. Merkle, J. G. and Corten, H. T., *Trans. ASME, J. Pres. Ves. Tech.*, **96**(4) (1974), pp. 286–92.
18. Ford, H. and Lianis, G., *Z. Angew. Math. Phys.*, **8** (1957), pp. 360–82.
19. Haigh, J. R. and Davenport, R. T., Unpublished work.
20. Irwin, G. R., Plastic zone near a crack tip and fracture toughness, *Proc. 7th Sagamore Conf. IV*, **63**, 1960.